

Numerical solutions of mild slope equation by generalized finite difference method

Ting Zhang ^{a,*}, Ying-Jie Huang ^a, Lin Liang ^a, Chia-Ming Fan ^b, Po-Wei Li ^b

^a Department of Water Resources and Harbor Engineering, College of Civil Engineering, Fuzhou University, China

^b Department of Harbor and River Engineering & Computation and Simulation CenterNational Taiwan Ocean University, Keelung 20224, Taiwan



ARTICLE INFO

Keywords:

Mild slope equation
Generalized finite difference method
Meshless method
Refraction
Diffraction
Coastal engineering

ABSTRACT

The mild slope equation (MSE) has been widely used to describe combined wave refraction and diffraction in the field of coastal and offshore engineering owing to its applicability for a wide range of wave frequencies. In this paper, a meshless numerical algorithm, based on the generalized finite difference method (GFDM), is firstly proposed to efficiently and accurately solve the MSE. As a newly-developed domain-type meshless method, the GFDM can truly get rid of time-consuming meshing generation and numerical quadrature. The partial differential terms of the MSE for each point in the computational domain can be discretized into linear combinations of nearby function values with the moving-least-squares method of the GFDM, so the numerical implementation is very convenient and efficient. To evaluate the accuracy and capability of the proposed scheme for MSE, a series of numerical tests were conducted, covering a range of complexity that included propagation and transformation of waves due to a parabolic shoal, a circular island mounted on a paraboloidal shoal and elliptic shoal situated on a slope, as well as breakwater gap. The results were compared with experimental data, analytical solutions and other numerical methods, and reasonable agreements have been achieved.

© 2017 Elsevier Ltd. All rights reserved.

1. Introduction

Wave propagation in various water depth usually accompany with refraction, diffraction and other wave transformations. These characteristics of wave motion will have significant influence on applications of coastal engineering, hence it is imperative to estimate the offshore wave conditions for coastal structure designing, sediment transport and economical operation. In 1972, assuming irrotational linear harmonic waves and ignoring energy loss due to friction or breaking, Berkhoff [1] derived the original mild slope equation (MSE) by integrating the Laplace equation over the water depth after multiplying a water depth function. Thereafter, the MSE has been widely used in the field of coastal engineering for its reliability in dealing with complex wave problem and its accuracy of describing combined refraction and diffraction phenomenon.

The original MSE is a single frequency wave equation based on linear wave theory, so many additional physical effects, which play essential roles in the wave transformations prediction, are not taken into account. To describe more realistic complex wave transformations, the original MSE has been improved by many researchers with different ways, such as taking into account the terms of fractional dissipation [2–4] and of steep slope [4–6], considering wave breaking [7,8] and

wave-current interaction [9,10], as well as extending the original MSE to include time element forming a time-dependent equation [11–13].

Since the equation is essentially the elliptic type with inseparable characteristics, presenting a direct solution to the original MSE is problematic. Therefore, various numerical methods have been proposed to solve the MSE. The iterative method, based on the conjugate-gradient (CG) technique, was developed by Panchang et al. [14], who used a preconditioning method to accelerate the speed of convergence in the solution process of solving the MSE. Moreover, a generalized conjugate method without using the preconditioning method was proposed by Li [15] to solve the MSE and achieved a result as good as Panchang's model. Tang et al. [16] combined the finite difference method (FDM) and the generalized product-type bi-conjugate gradient (GPBiCG) method to simulate wave propagating in the near shore region. Chen et al. [17] used a finite element coastal wave method to simulate the wave-current interaction phenomenon by solving an extended mild slope wave current equation. Besides, a numerical model is developed by Liu et al. [18] based on the preconditioned self-adaptive finite element model (FEM) to solve the MSE. In addition, Naserizadeh et al. [19] used the boundary element method (BEM) and a high-order FDM conjunctively to solve the modified MSE. However, each of these methods has advantages and disadvantages for the applicability, accuracy and stability, as well as computational cost when dealing with different equation.

* Corresponding author.

E-mail address: zhangting@fzu.edu.cn (T. Zhang).

Over the past few decades, the conventional mesh-based methods have been developed quite perfectly. Nevertheless, in some cases such as the complex-geometry and higher dimensional problems, mesh generation and numerical integration need considerable amount of time and thus decrease computational efficiency greatly. Being regarded as a promising alternative to classical mesh-based methods, the meshless methods have the potential to avoid the problem of domain or surface grid generation and numerical quadrature. Since it was put forward, the meshless numerical schemes have been gradually derived a series of methods such as the method of fundamental solutions (MFS) [20,21], the smoothed-particle hydrodynamics (SPH) [22], the element-free Galerkin method (EFGM) [23], the modified collocation Trefftz method (MCTM) [24,25], the meshless local Petrov–Galerkin method (MLPGM) [26], the local radial basis function collocation method (LRBFCM) [27] and the generalized finite difference method (GFDM) [28–38].

Within the above meshless methods, the GFDM belongs to a domain-type one, since both of boundary nodes and interior nodes are simultaneously adopted in numerical implementation. In the GFDM, by utilizing the weighted least squares fitting technique and Taylor series expansion, the derivatives of the unknown variables for each point in the computational domain can be discretized into linear combinations of nearby function values with different weighting coefficients, then a sparse system of nonlinear algebraic equations is yielded and can be efficiently solved by using various sparse matrix solvers. This feature makes the GFDM easy-to-program, straightforward and efficient when applied to a large and complicated computational region. Benito et al. [28] derived the explicit formulas of the GFDM and some influencing factors on numerical accuracy were discussed with several sets of mathematical cases. Thereafter, Gavette et al. [31] improved the GFDM and obtained satisfying results by comparing with other meshless methods. For over a decade, the GFDM has been gradually applied on various mathematical problems. Benito et al. [29,30] applied the GFDM to solve parabolic and hyperbolic equations and improved the approximated solution of partial difference equations. More challenging, the GFDM is used to solve third-and fourth-order partial differential equations by Urena et al. [32]. Recent advances, which enable approximation of nonlinear conditions, have the potential to extend the GFDM for various scientific and engineering applications. Chan et al. [33] utilized the GFDM and a newly-developed solver for nonlinear algebraic equation to deal with two-dimensional nonlinear obstacle problems, while Fan et al. [34,35] applied the GFDM on inverse biharmonic boundary-value problems and two-dimensional Cauchy problems. Zhang et al. [36,37] adopted the GFDM to simulate the two dimensional sloshing phenomenon and the propagation of nonlinear water waves in numerical wave flume. Li and Fan [38] utilized the GFDM to analyze the two-dimensional shallow water equation.

In this paper, we investigated a meshless numerical scheme, based on the GFDM, for solving the wave transformation processes in nearshore region, including diffraction, refraction, reflection, and weak nonlinearity, which is governed by the MSE. The proposed GFDM-based model is truly free from mesh generation and numerical quadrature, so it is very effective, simple and accurate to deal with problems in irregular domains, governed by the MSE. It should be noted that, as described above, the GFDM has been recently applied to various partial differential equations (PDEs). To the best of our knowledge, this is the first time that the GFDM is applied for accurately solving the MSE. In addition, this paper focuses on numerical solution of nonlinear equations, although many published GFDM-related papers mainly investigated numerical solutions of linear PDEs. Besides, the flexibility of the GFDM is also emerged since the spatial derivatives at any position can be easily acquired by the GFDM. It is worthwhile to mention that, for much shorter period of incident wave, the computational cost for most numerical method will substantially increase due to sufficient accuracy. This situation is a challenging test for any numerical model. A surprising result is obtained in the present paper. Furthermore, the accuracy of the MSE models is carefully verified in the way for

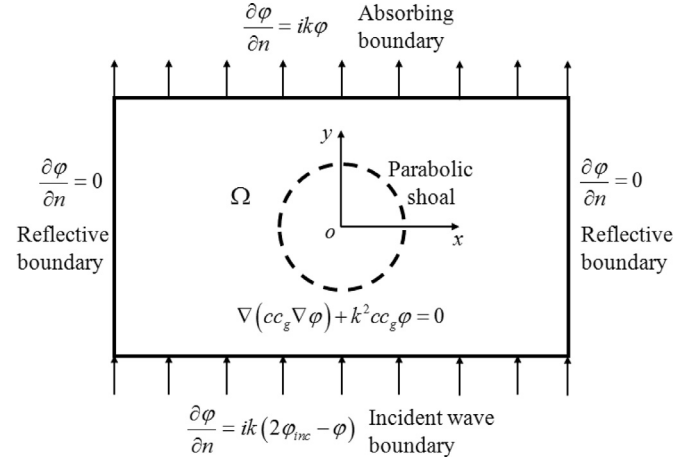


Fig. 1. Schematic diagram of computational domain and boundary conditions in this study.

linear and nonlinear dispersion relations. Four numerical examples, including refraction of long waves over a parabolic shoal, wave around a circular island on a paraboloidal shoal and wave propagation over an elliptic shoal, as well as single gate breakwater, are provided to assess the merits of using the GFDM for numerical solutions of the MSE. In addition, some correlation parameters are investigated to verify the stability and convergence of the proposed meshless numerical scheme.

2. Governing equation and boundary conditions

2.1. Governing equations

When a homogeneous incompressible fluid with irrotational motion travels over a sea bottom with variable depth $h(x, y)$, diffraction and reflection usually occur due to shoals or solid boundaries. Thus, the fluid can be expressed in terms of the velocity potential $\Phi(x, y, z, t)$, which satisfies the Laplace equation as follow [1],

$$\nabla^2 \Phi + \frac{\partial^2 \Phi}{\partial z^2} = 0 \quad -h(x, y) \leq z \leq 0 \quad (1)$$

The linear free surface boundary conditions for harmonic waves is,

$$\frac{\partial \Phi}{\partial z} + \frac{\omega^2}{g} \Phi = 0 \quad z = 0 \quad (2)$$

The kinematic boundary condition at the impermeable bottom is,

$$\frac{\partial \Phi}{\partial z} + \nabla h \cdot \nabla \Phi = 0 \quad z = -h(x, y) \quad (3)$$

Where x, y denote the horizontal coordinates while z is the vertical coordinate measured positively upwards with the undisturbed free surface at $z=0$. $\nabla = (\frac{\partial}{\partial x}, \frac{\partial}{\partial y})$ is used to indicate the horizontal gradient operator and g denotes the gravitational acceleration.

For monochromatic waves, the velocity potential $\Phi(x, y, z, t)$ can be presented as [39],

$$\Phi(x, y, z, t) = \text{Re}\{\varphi(x, y)f(z)e^{-i\omega t}\} \quad (4)$$

in which symbol Re represents the real part of a complex value and φ is the two-dimensional complex horizontal wave velocity potential of the water surface. $f(z)$ is the depth dependency, provided by

$$f(z) = \frac{\cosh[k(h+z)]}{\cosh(kh)} \quad (5)$$

where $k = k(x, y)$ denotes the local wave number.

Referring to Fig. 1, a Cartesian coordinate system is adopted, in which the horizontal coordinate (x, y) is located at the still water

surface. To get an equation for the two-dimensional function φ , Laplace equation is integrated with respect to water depth from sea bottom to free surface after multiplication with the function $f(z)$. The MSE, which was originally derived by Berkhoff in 1972[1], can be expressed as,

$$\nabla(cc_g\nabla\varphi)+k^2cc_g\varphi=0 \quad (6)$$

$$H=\frac{2\omega}{g}\sqrt{\phi_1^2+\phi_2^2} \quad (7)$$

in which $c=\omega/k$ and $c_g=n'\omega/k$ stand for the phase and group velocity, respectively, where ω is the regular frequency and $n'=0.5(1+2kh/\sinh 2kh)$ denotes the shoaling factor. The two-dimensional complex horizontal wave velocity potential $\varphi=\varphi_1+i\varphi_2$ with $i=\sqrt{-1}$, in which φ_1 and φ_2 denote the real and imaginary part of the complex wave velocity potential, respectively. H represents the wave height.

The wave number k may be determined through the linear dispersion relation,

$$\omega^2=gk\tanh(kh) \quad (8)$$

To increase accuracy for most practical applications, the dispersion equation has been modified to contain the nonlinear effects of wave motion, which leads to modification of the phase and group velocities [40]. The modified form of the dispersion equation is depicted as follows:

$$\omega^2=gk[1+(ka)^2F_1\tanh^5(kh)]\tanh[kh+(ka)F_2] \quad (9)$$

where $a=H/2$ designates the wave amplitude. The function F_1 and F_2 are defined as,

$$F_1=\frac{\cosh(4kh)+8-2\tanh^2(kh)}{8\sinh^4(kh)} \quad (10)$$

$$F_2=\left(\frac{kh}{\sinh kh}\right)^4 \quad (11)$$

When considered the nonlinear dispersion relationships, the solution of the current formulation is an iterative process, which will be illustrated in the Section 3.2.

2.2. Boundary conditions

Suitable boundary conditions for the closed and open boundaries are significantly important to the MSE, which have been discussed by many researchers [14–16,41]. A physical boundary, characterized by a specified reflection coefficient, can either fully absorb or partially or fully reflect approaching waves [17]. In this paper, detailed descriptions of boundary conditions for the application types are presented below.

The incident boundary condition is usually assigned to incorporate both the incident wave potential φ_{inc} and the effect of reflected waves leaving the offshore boundary. It is specified along the boundary as depicted in Fig. 1 and is presented as,

$$\frac{\partial\phi}{\partial n}=ik(2\phi_{inc}-\phi) \quad (12)$$

where n denotes the outward normal to the boundary, $\phi_{inc}=\frac{2kag}{\omega}e^{-kx}$.

In addition to the offshore boundary condition, fully absorbing, partially absorbing and fully reflective boundary conditions are defined with a universal form as follow:

$$\frac{\partial\phi}{\partial n}=ik\alpha\phi \quad (13)$$

where α , the defined reflection coefficient, changes within the range of 0–1 depending on the boundary situation and may be determined empirically. $\alpha=0$ is a fully reflective boundary, which means that the propagated waves can be fully reflected by a vertical sea wall as shown in Fig. 1 for the lateral boundaries, while $\alpha=1$ implies a fully absorbing one, along which there are only outgoing waves, as the upper boundary illustrated in Fig. 1. In addition, waves may be partially reflected by a gravel beach for $0 < \alpha < 1$ in some special cases.

3. Numerical methods

3.1. The GFDM

The numerical procedures of the GFDM for two-dimensional problem with boundary conditions are briefly introduced in this subsection. In the GFDM, the moving-least-squares method is adopted to derive the expressions of spatial derivatives.

At beginning, a set of boundary nodes and interior nodes are distributed arbitrarily or uniformly in the computational domain. For a given i th node, there is a star formed by n_s nearest nodes around it and itself. Taylor series is used to expand the function within the star and a new functional, $B(\mathbf{D}_u)$, is defined as follows [28–37,42],

$$B(\mathbf{D}_u)=\sum_{j=1}^{n_s}\left\{\left(\phi_i-\phi_j^i+\mathbf{e}_{ij}^T\mathbf{D}_u\right)w_{ij}\right\}^2 \quad (14)$$

where $\mathbf{D}_u=(\frac{\partial\phi}{\partial x}|_i\frac{\partial\phi}{\partial y}|_i\frac{\partial^2\phi}{\partial x^2}|_i\frac{\partial^2\phi}{\partial y^2}|_i\frac{\partial^2\phi}{\partial x\partial y}|_i)^T$ is the vector of unknown derivatives at the i th node and $\mathbf{e}_{ij}=(h_{ij}\ k_{ij}\ \frac{h_{ij}^2}{2}\ \frac{k_{ij}^2}{2}\ h_{ij}k_{ij})^T$. j is the local index in the star and $\{x_j^i, y_j^i\}_{j=1}^{n_s}$ denote the coordinates of the n_s nodes. $h_{ij}=x_i-x_j^i$ and $k_{ij}=y_i-y_j^i$ stand for the distances between the i th node and the j th node along x and y directions, respectively. $w_{ij}=w(h_{ij}, k_{ij})$ is the value of weighting function at (x_j^i, y_j^i) . A variety of weighting functions have been proposed in the past researches [28–32], such as potential function, cubic spline and quartic spline etc. The quartic spline, which is chosen as the weighting function in this study, can be expressed as,

$$w(d_{ij})=\begin{cases} 1-6\left(\frac{d_{ij}}{dm_i}\right)^2+8\left(\frac{d_{ij}}{dm_i}\right)^3-3\left(\frac{d_{ij}}{dm_i}\right)^4 & d_{ij} \leq dm_i, \\ 0 & d_{ij} > dm_i \end{cases} \quad (15)$$

where d_{ij} denotes the distance between the i th node and the j th node. dm_i is the distance between the i th node and the farthest node within the star, also specified as the radius of the star.

Making $\nabla B(\varphi)=\mathbf{0}$, in order to minimize the function, a system of linear equations can be obtained as follows:

$$\mathbf{AD}_u=\mathbf{b} \quad (16)$$

where

$$\mathbf{A}=\sum_{j=1}^{n_s}w_{ij}^2\mathbf{e}_{ij}\mathbf{e}_{ij}^T \quad (17)$$

$$\mathbf{b}=\sum_{j=1}^{n_s}w_{ij}^2\left(\phi_i-\phi_j^i\right)\mathbf{e}_{ij} \quad (18)$$

In consequence, \mathbf{D}_u can be obtained as the following equation,

$$\mathbf{D}_u=\mathbf{A}^{-1}\mathbf{b}=\mathbf{A}^{-1}\sum_{j=1}^{n_s}w_{ij}^2\phi_i\mathbf{e}_{ij}-\mathbf{A}^{-1}\sum_{j=1}^{n_s}w_{ij}^2\phi_j^i\mathbf{e}_{ij}=-\mathbf{p}_0^i\phi_j^i+\sum_{j=1}^{n_s}\mathbf{p}_j^i\phi_i \quad (19)$$

in which

$$\mathbf{p}_0^i=\sum_{j=1}^{n_s}\mathbf{A}^{-1}w_{ij}^2\mathbf{e}_{ij} \quad (20)$$

$$\mathbf{p}_j^i=\mathbf{A}^{-1}w_{ij}^2\mathbf{e}_{ij} \quad (21)$$

The spatial derivatives at the i th node can be rewritten as a linear combination system of other physical values multiplying the corresponding weighting coefficients. Since these formulas were derived by using the second-order Taylor series expansion, the theoretically minimum value for n_s is 5 to ensure the existence of inverse of matrix \mathbf{A} in Eq. (19) [28,31]. In the light of our previous research experiences [33–38], the numerical simulation for second-order partial differential

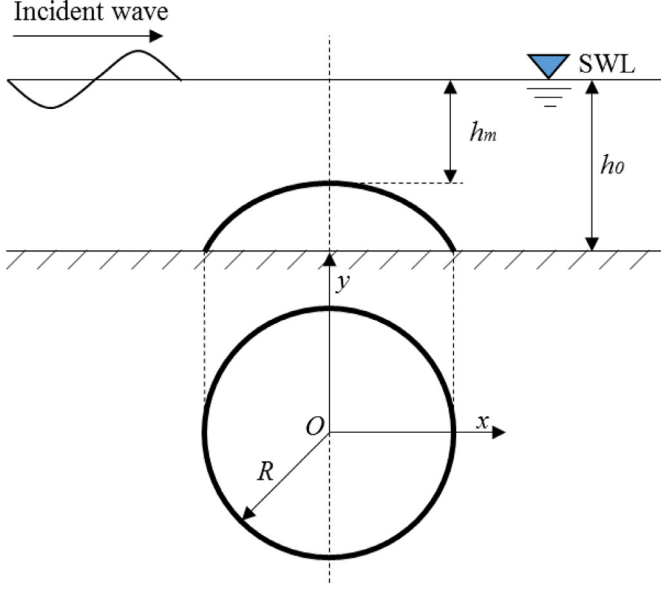


Fig. 2. Definition sketch of wave refraction over parabolic shoal.

equation will get a more favorable result for a n_s larger than 10. In consideration of the MSE is a second-order partial differential equation, the adopted value of n_s for all the numerical examples in this paper is 10.

To express the spatial derivatives in a straightforward way, \mathbf{D}_u can be rewritten as follows:

$$\frac{\partial \phi}{\partial x} \Big|_i = p_0^{x,i} \phi_i + \sum_{j=1}^{n_s} p_j^{x,i} \phi_j^i \quad (22)$$

$$\frac{\partial \phi}{\partial y} \Big|_i = p_0^{y,i} \phi_i + \sum_{j=1}^{n_s} p_j^{y,i} \phi_j^i \quad (23)$$

$$\frac{\partial^2 \phi}{\partial x^2} \Big|_i = p_0^{xx,i} \phi_i + \sum_{j=1}^{n_s} p_j^{xx,i} \phi_j^i, \quad (24)$$

$$\frac{\partial^2 \phi}{\partial y^2} \Big|_i = p_0^{yy,i} \phi_i + \sum_{j=1}^{n_s} p_j^{yy,i} \phi_j^i, \quad (25)$$

$$\frac{\partial^2 \phi}{\partial x \partial y} \Big|_i = p_0^{xy,i} \phi_i + \sum_{j=1}^{n_s} p_j^{xy,i} \phi_j^i, \quad (26)$$

where $\{p_j^{x,i}\}_{j=0}^{n_s}$, $\{p_j^{y,i}\}_{j=0}^{n_s}$, $\{p_j^{xx,i}\}_{j=0}^{n_s}$, $\{p_j^{yy,i}\}_{j=0}^{n_s}$, $\{p_j^{xy,i}\}_{j=0}^{n_s}$ are coefficients corresponding to the i th node. Readers can refer to some published papers about the GFDM for more detailed descriptions since the above derivational procedure have been clearly described by some authors [28–38]. In order to acquire the expressions for spatial derivatives of every arranged node, the above-described procedures should be applied to each node when it is regarded as the i th node. To yield a system of linear algebraic equations for acquiring the numerical solution, every interior node should meet the governing equation and each boundary node should satisfy the boundary condition. As has been described, the numerical procedure of the GFDM is simple, straightforward and easily understandable.

3.2. Solving the MSE with the GFDM

Since four cases with different boundary conditions will be introduced in this paper, the universal procedures to solve the MSE using the GFDM will be illustrated in this subsection referring to Fig. 1. n_i nodes are distributed inside computational domain, and $n_{b1}, n_{b2}, n_{b3}, n_{b4}$ nodes

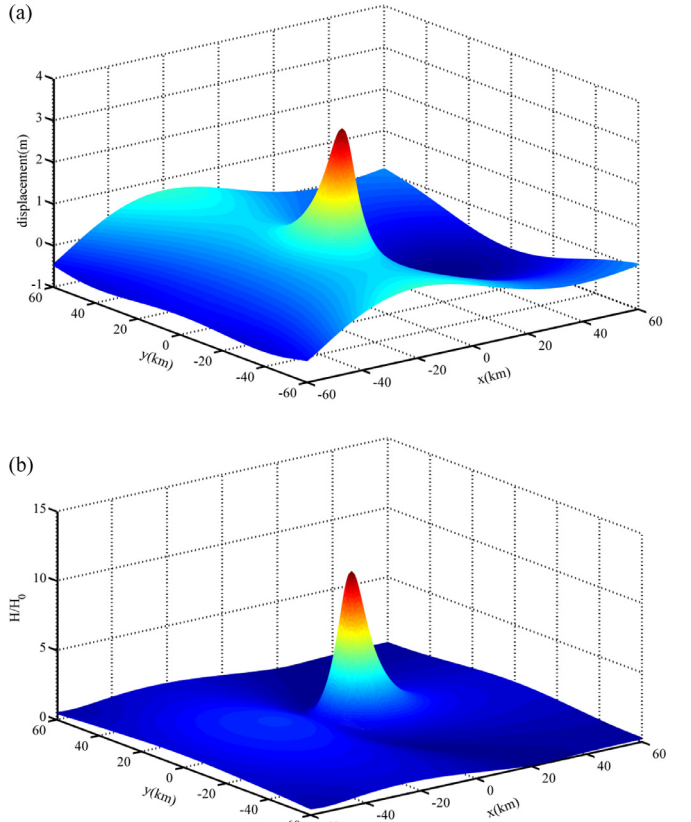


Fig. 3. 3-D presentation of results for parabolic shoal. (a) free surface elevation, and (b) relative wave height.

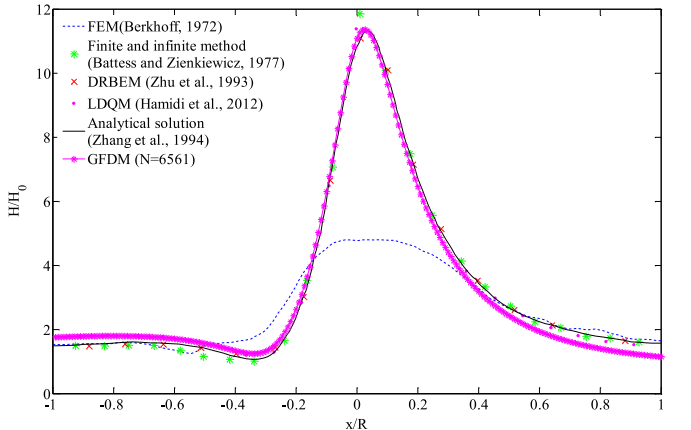


Fig. 4. Comparison of relative wave amplification along $y=0$ between the GFDM and other solution methods.

are distributed along incident wave boundary, right reflective boundary, absorbing boundary and left reflective boundary, respectively. By performing the procedures as Eqs. (14)–(21), the expressions of spatial derivatives for all nodes can be discretized into linear combinations of nearby function values with the form of Eqs. (22)–(26). With this thinking, Eq. (6) can be rewritten in scalar as follows:

$$\frac{\partial(cc_g)}{\partial x} \frac{\partial \varphi}{\partial x} + \frac{\partial(cc_g)}{\partial y} \frac{\partial \varphi}{\partial y} + cc_g \left(\frac{\partial^2 \varphi}{\partial x^2} + \frac{\partial^2 \varphi}{\partial y^2} \right) + k^2 cc_g \varphi = 0 \quad (27)$$

A system of n_i linear algebraic equations taking the following form can be yielded by imposing the satisfactions of governing equation at

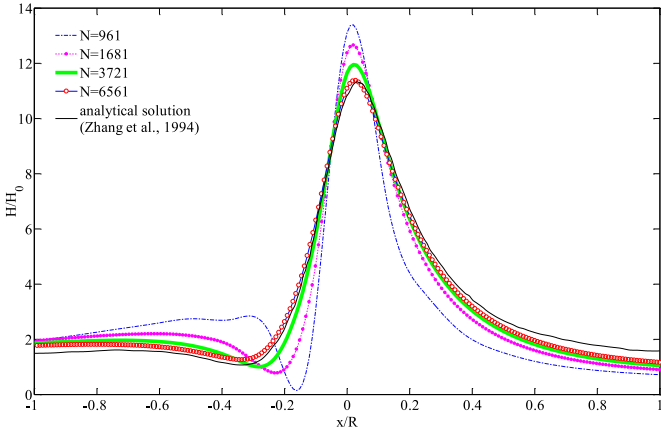


Fig. 5. Profiles of GFDM solutions by using different numbers of total nodes.

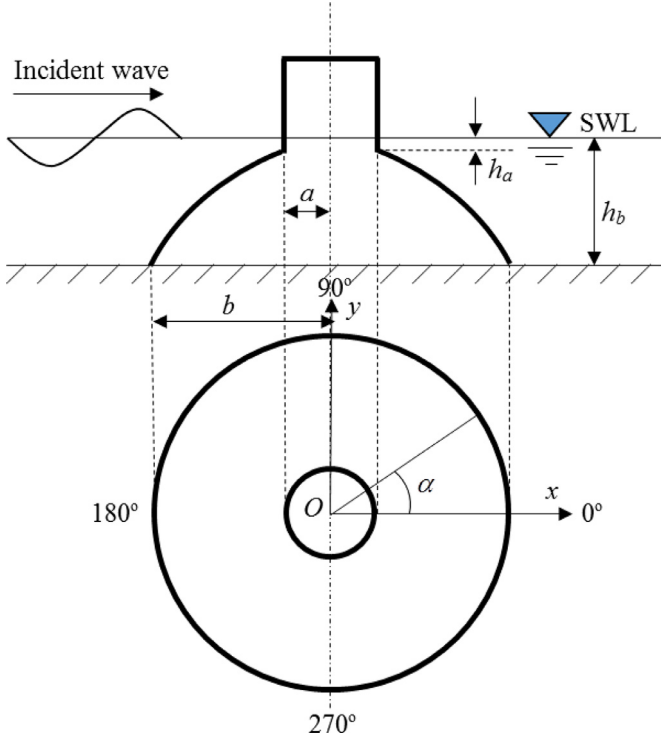


Fig. 6. Definition sketch of original Homma's island.

every interior node,

$$\begin{aligned} & \left(p_0^{x,i} (cc_g)_i + \sum_{j=1}^{n_s} p_j^{x,i} (cc_g)_j \right) \left(p_0^{x,i} \phi_i + \sum_{j=1}^{n_s} p_j^{x,i} \phi_j^i \right) \\ & + \left(p_0^{y,i} (cc_g)_i + \sum_{j=1}^{n_s} p_j^{y,i} (cc_g)_j \right) \left(p_0^{y,i} \phi_i + \sum_{j=1}^{n_s} p_j^{y,i} \phi_j^i \right) \\ & + (cc_g)_i \left(p_0^{xx,i} \phi_i + \sum_{j=1}^{n_s} p_j^{xx,i} \phi_j^i + p_0^{yy,i} \phi_i + \sum_{j=1}^{n_s} p_j^{yy,i} \phi_j^i \right) i = 1, 2, 3, \dots, n_i \\ & + k^2 (cc_g)_i \phi_i = 0 \end{aligned} \quad (28)$$

Moreover, to enforce the satisfactions of the boundary conditions along all boundaries will generate the following linear algebraic equations system,

$$\begin{aligned} & \frac{\partial \phi}{\partial y} \Big|_i = p_0^{y,i} \phi_i + \sum_{j=1}^{n_s} p_j^{y,i} \phi_j^i = ik(2\phi_{inc} - \phi) \\ & i = n_i + 1, n_i + 2, n_i + 3, \dots, n_i + n_{b1} \end{aligned} \quad (29)$$

$$\begin{aligned} & \frac{\partial \phi}{\partial x} \Big|_i = p_0^{x,i} \phi_i + \sum_{j=1}^{n_s} p_j^{x,i} \phi_j^i = 0 \\ & i = n_i + n_{b1} + 1, n_i + n_{b1} + 2, n_i + n_{b1} + 3, \dots, n_i + n_{b1} + n_{b2} \end{aligned} \quad (30)$$

$$\begin{aligned} & \frac{\partial \phi}{\partial y} \Big|_i = p_0^{y,i} \phi_i + \sum_{j=1}^{n_s} p_j^{y,i} \phi_j^i = ik\phi \\ & i = n_i + n_{b1} + n_{b2} + 1, n_i + n_{b1} + n_{b2} + 2, n_i + n_{b1} + n_{b2} \\ & + 3, \dots, n_i + n_{b1} + n_{b2} + n_{b3} \end{aligned} \quad (31)$$

$$\begin{aligned} & -\frac{\partial \phi}{\partial x} \Big|_i = p_0^{x,i} \phi_i + \sum_{j=1}^{n_s} p_j^{x,i} \phi_j^i = 0 \\ & i = n_i + n_{b1} + n_{b2} + n_{b3} + 1, n_i + n_{b1} + n_{b2} + n_{b3} + 2, \dots, N \end{aligned} \quad (32)$$

where $N = n_i + n_{b1} + n_{b2} + n_{b3} + n_{b4}$ denotes the number of total nodes.

Finally, a sparse system of linear algebraic equations can be yielded by combining Eqs. (28)–(32) as follows:

$$[\mathbf{E}]_{N \times N} \{\phi\}_{N \times 1} = \{\mathbf{g}\}_{N \times 1} \quad (33)$$

where $[\mathbf{E}]$ is a sparse coefficient matrix, which can be efficiently solved. The sparsity of $[\mathbf{E}]$ is due to that every node is related to only 10 nodes within the star mentioned before. $\{\mathbf{g}\}$ contains both the boundary data and the homogeneous terms of the governing equation. The numerical solutions of velocity potential at every node inside computational domain and along every boundary segment can be acquired by solving Eq. (33).

In this paper, four classical numerical examples were provided to verify the merits of the proposed meshless scheme. The control equation in the former two cases is the MSE with linear dispersion relations, while in the last two cases, the control equation is with either linear or nonlinear dispersion relations. The nonlinear dispersion relationships can be solved with an iterative procedure. In the first step, the wave height H is computed with Eqs. (33), (7) and (8). Then, k can be estimated using Eq. (9). By substituting the modified k , which incorporates nonlinear effects, into the Eqs. (33) and (7), an updated distribution for H is obtained. This iterative procedure does not cease until the wave number has a slight disparity with the previous iteration. This form of the MSE is referred to the nonlinear model after above modified process. As pointed out by previous researchers [14,43,44], the nonlinear model can lead to more accurate results than linear model. In this paper, the dominant nonlinear effects between the linear and nonlinear model will also be discussed in subsequent sections.

As described above, the proposed meshless numerical scheme is simple and easy-to-program. The combined diffraction and refraction problem described by the MSE, which contains partial differential term, can be analyzed by the GFDM. Four numerical examples will be provided to verify the advantages of the proposed numerical scheme in the next section.

4. Numerical results and comparisons

In order to verify the feasibility and accuracy of solving the MSE with the GFDM, four numerical examples, such as long wave propagation over a parabolic shoal [1,39,45–47], wave scattering by Homma's island [48–53] and wave propagation over an elliptic shoal [14,16,43,47,54], as well as wave propagation after a single gate breakwater [16,47,55], are simulated in this section. The numerical results adopted by the proposed meshless method will be validated by comparing with experimental data, other numerical results and analytical solution.

4.1. Long wave propagation over a parabolic shoal

Long wave propagation over a parabolic shoal is studied in the first example. This case was firstly proposed and solved numerically with

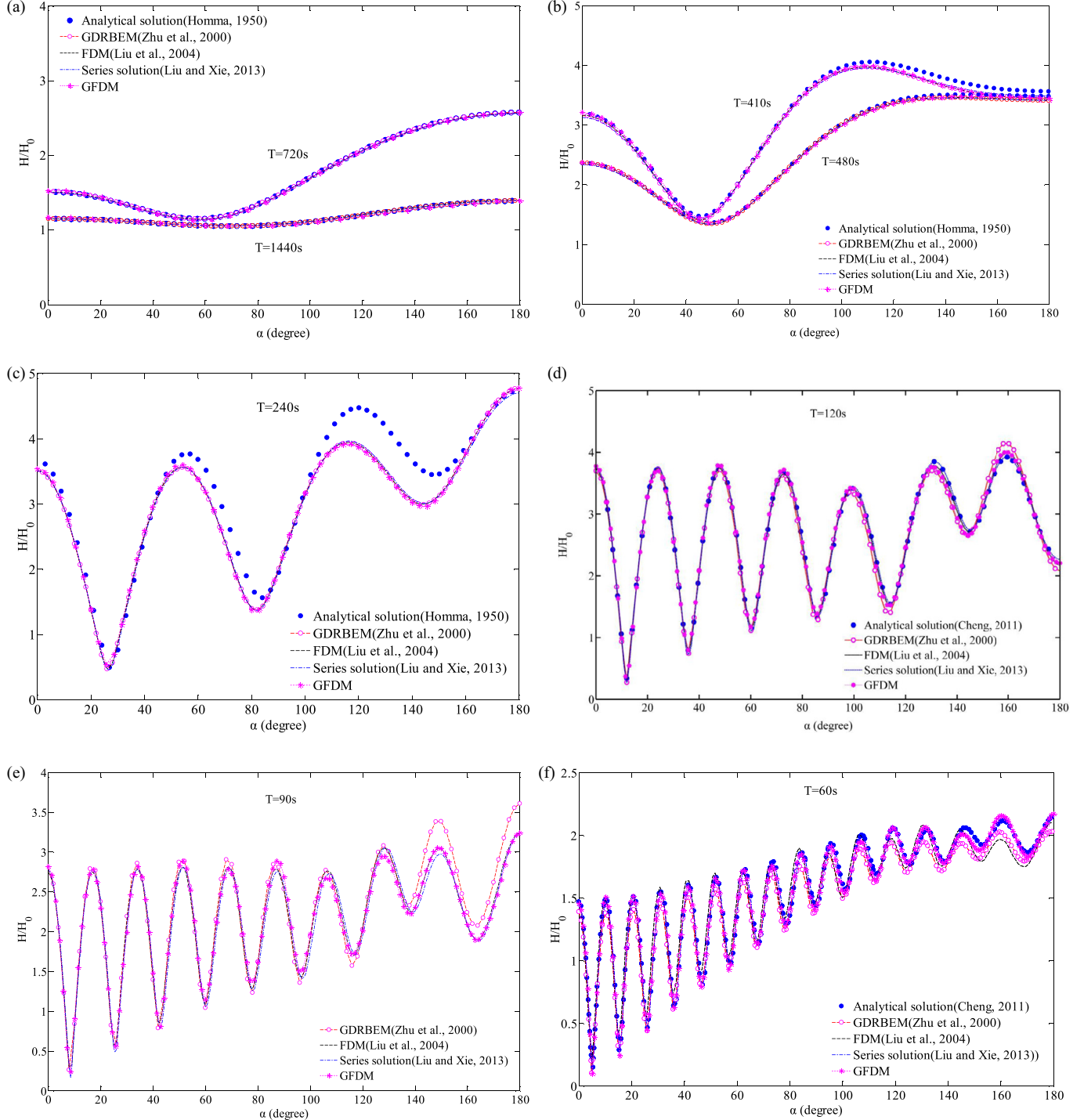


Fig. 7. Comparison of solutions of wave amplification along coastline of original Homma's island. (a) $T = 1440\text{ s}$ ($k_a h_a = 0.0294$ and $k_b h_b = 0.0883$) and $T = 720\text{ s}$ ($k_a h_a = 0.0559$ and $k_b h_b = 0.1772$), (b) $T = 480\text{ s}$ ($k_a h_a = 0.0883$ and $k_b h_b = 0.2676$) and $T = 410\text{ s}$ ($k_a h_a = 0.1034$ and $k_b h_b = 0.3146$), (c) $T = 240\text{ s}$ ($k_a h_a = 0.1772$ and $k_b h_b = 0.5549$), (d) $T = 120\text{ s}$ ($k_a h_a = 0.3601$ and $k_b h_b = 1.2990$), (e) $T = 90\text{ s}$ ($k_a h_a = 0.4882$ and $k_b h_b = 2.0555$) and (f) $T = 60\text{ s}$ ($k_a h_a = 0.7693$ and $k_b h_b = 4.4772$).

FEM by Berkhoff [1]. Later, Bettess and Zienkiewicz [45] simulated this example with finite and infinite method and acquired different results with those of Berkhoff. After two decades, Zhu et al. [39] proved that Bettess and Zienkiewicz's results are correct with dual reciprocity boundary element method (DRBEM). Then, an analytical solution was presented by Zhang and Zhu [46]. The geometry of this example is depicted in Fig. 2. The variation of water depth h is defined as,

$$\begin{cases} h = h_m(1 + \beta r^2) & r \leq R \\ h = h_0 & r > R \end{cases} \quad (34)$$

where $h_m = 50\text{ m}$ and $h_0 = 4000\text{ m}$ denote the water depth of the shoal top and the sea bed, respectively. Then $\beta = (h_0 - h_m)/h_m$ is 79. $R = 33,000\text{ m}$ is the shoal radius and dimensionless incident wavelength $\lambda_0/R = 4.32$. r is horizontal distance between the shoal center and the calculated point.

In this case, the incident wave is defined as formula (12) and other three boundaries are defined as absorbing boundary conditions

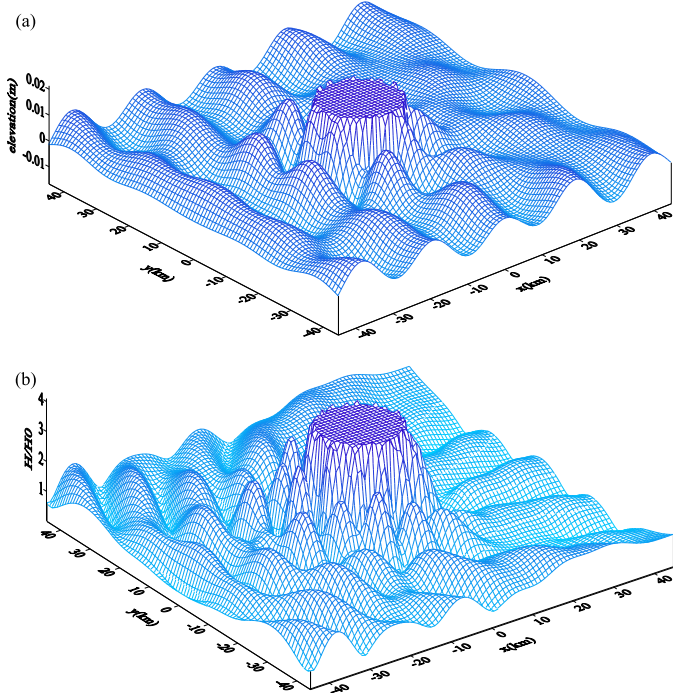


Fig. 8. 3-D presentation of results for Homma's island case for $T = 240$ s. (a) free surface elevation, and (b) relative wave height.

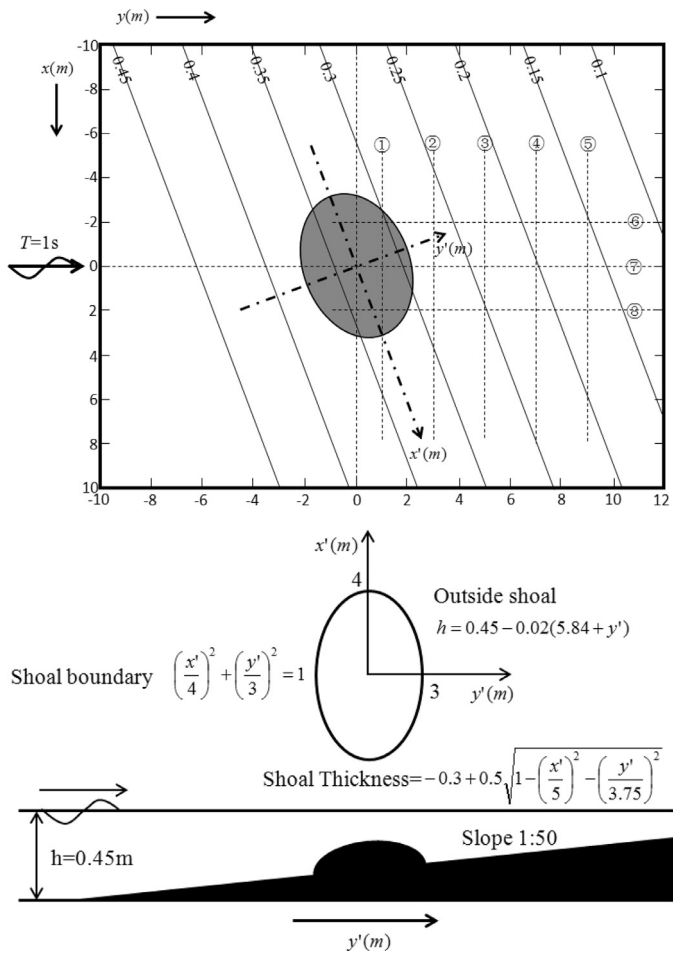


Fig. 9. Schematic view of experimental model of elliptic shoal (Berkhoff et al., 1982).

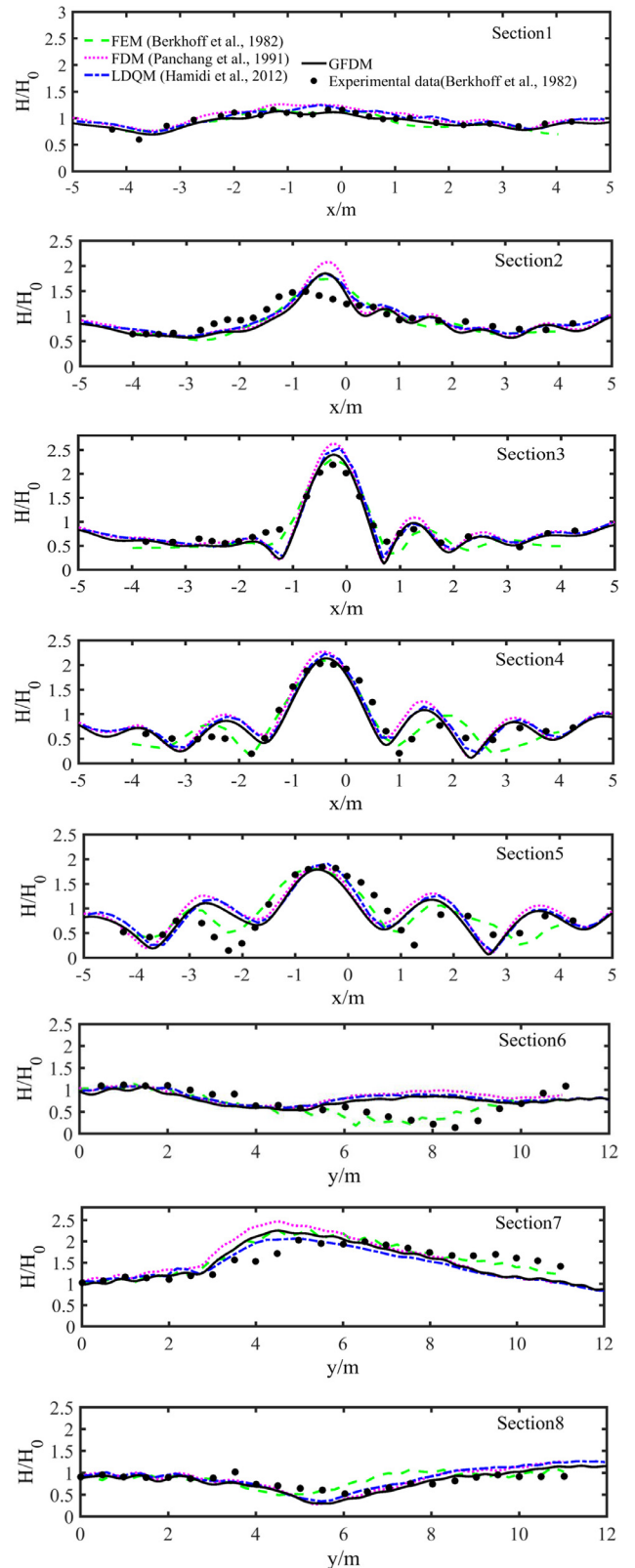


Fig. 10. Comparison of linear GFDM results with experimental data and other numerical results.

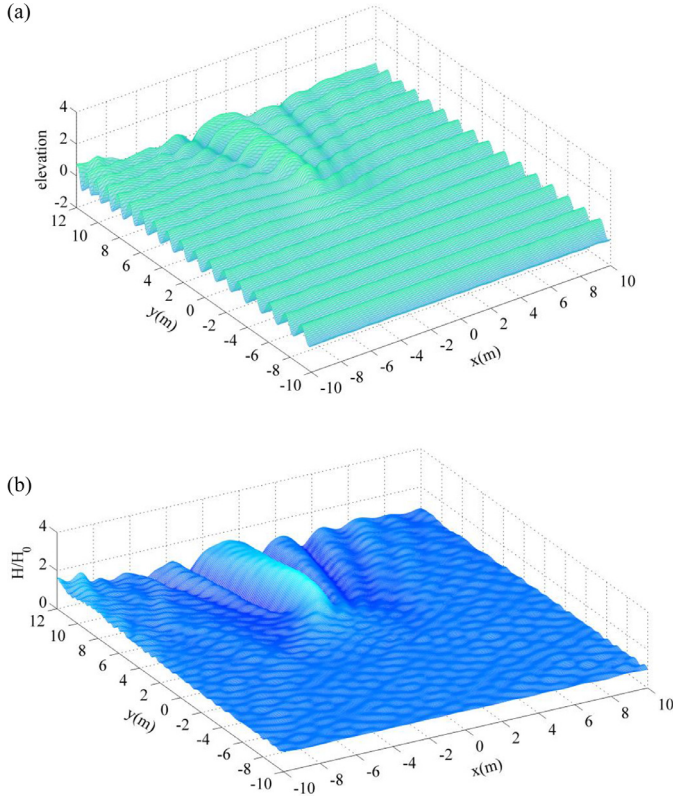


Fig. 11. 3-D presentation of results for elliptic shoal model. (a) free surface elevation, and (b) relative wave height.

described as formula (13) with $\alpha=1$ since the shoal is surrounded by infinite area. The computational domain is $-60 \text{ km} \leq x, y \leq 60 \text{ km}$.

Fig. 3 demonstrates a three-dimensional presentation of wave motion such as the profiles of free surface and the distributions of relative wave height in the entire simulated domain. The phenomena of long waves being refracted and diffracted are sequentially and accurately acquired with proposed method. It indicates that waves are greatly amplified owing to the shoaling of the water depth toward the center of the shoal and wave rays converge to form caustics in the lee region where the diffraction effects are significant.

For further validation, the numerical result by GFDM of wave amplification along $y=0$ is compared with other numerical results and analytical solution [1,39,45–47] as illustrated in Fig. 4. Except for Berkhoff's result [1], excellent agreements among the GFDM result and other solutions are observed. Moreover, the GFDM result and analytical solution are almost overlapped near the peak of the profile.

To analyze the stability and convergence of the proposed numerical scheme, the computational domain is discretized with four sets of total nodes $N = 961, 1681, 3721$ and 6561 , respectively. The comparison of four numerical results is revealed in Fig. 5. The analytical solution adopted by Zhang and Zhu [46] is also plotted in Fig. 5. Sensitivity tests showed the numerical results converge to analytical solution with the increasing of total nodes, and 6561 nodes can provide converging numerical results that are almost identical to the analytical solution.

According to above comparisons, the convergence and stability of the GFDM and the feasibility and accuracy of applying the GFDM to solve the MSE in this parabolic shoal case are verified.

4.2. Wave scattering by Homma's island

Wave scattering by Homma's island, which is designed and analytically solved by Homma based on long-wave equation (LWE) in 1950, is adopted as the second example in this subsection. This case has been

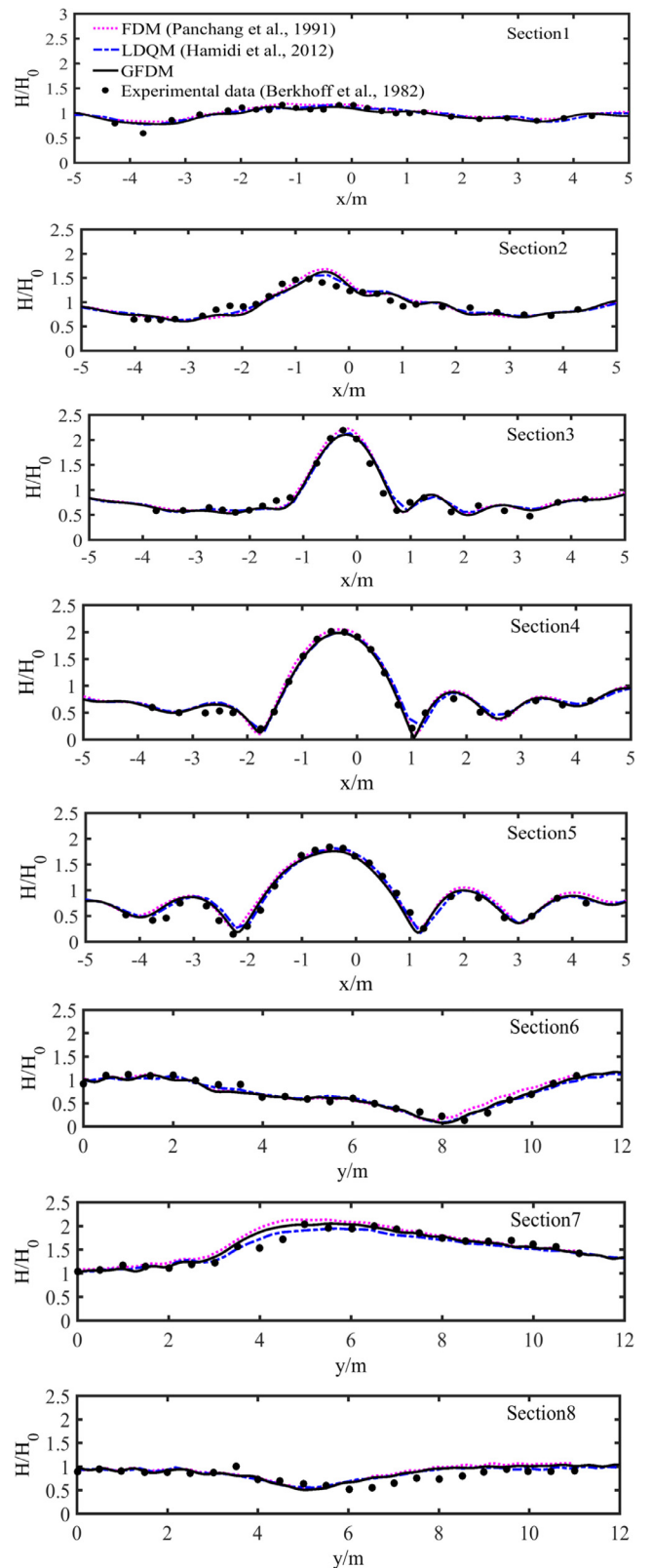


Fig. 12. Comparison of nonlinear GFDM results with experimental data and other numerical results.

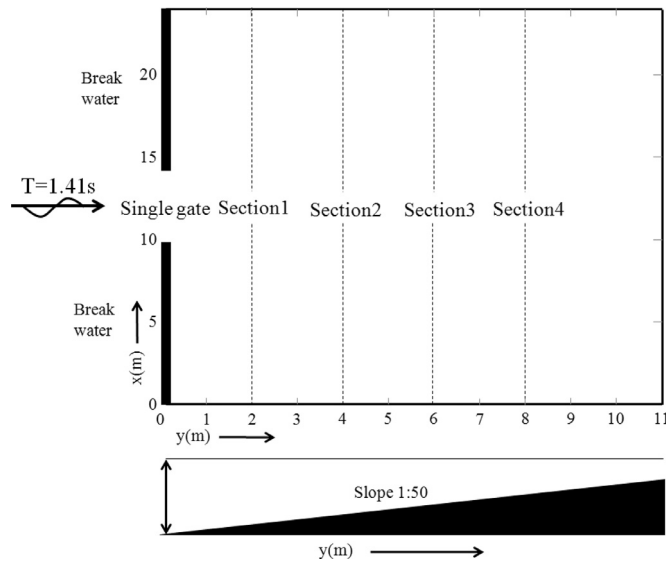


Fig. 13. Schematic view of topography and computation domain for breakwater gap (Wu and Xia, 1994).

presented to verify numerical methods by some researchers based on various equations including two major types. One is based on shallow water equation (SWE) such as Vastano and Reid's finite difference model [56], Berkhoff's finite element model combined with a source distri-

bution method [1] and Bettess and Zienkiewicz's hybrid finite element model [45]. The others are based on the MSE [39,49–53,57–59].

As demonstrated in Fig. 6, waves are diffracted and refracted by a structure named Homma's island, which is composed with a circular cylindrical island mounted on a paraboloidal shoal and is surrounded by infinite open sea. The water depth h is constant out of the shoal and varies on the shoal along the radial direction, described as follows:

$$h = \begin{cases} \frac{h_b}{b^2} \times r^2, & a \leq r \leq b \\ h_b, & r > b \end{cases} \quad (35)$$

where r denotes the horizontal distance between the center of the paraboloidal shoal and calculated point. $a = 10$ km and $b = 30$ km are radius of the island and the shoal, respectively. $h_b = 4$ km stands for the constant water depth out of the shoal. Then, $h_a = h_b/9$ is the water depth at the boundaries of the island and α denotes the angle that the calculated point deviates from the x direction as shown in Fig. 6.

In this subsection, the wave amplifications along the coastline for various incident wave periods ($T = 1440, 720, 480, 410, 240, 120, 90$ and 60 s) are simulated.

The incident waves with periods of $T = 1440$ s ($k_a h_a = 0.0294$ and $k_b h_b = 0.0883$), $T = 720$ s ($k_a h_a = 0.0559$ and $k_b h_b = 0.1772$), $T = 480$ s ($k_a h_a = 0.0883$ and $k_b h_b = 0.2676$), and $T = 410$ s ($k_a h_a = 0.1034$ and $k_b h_b = 0.3146$) are belonged to the long-wave range. The amplifications of those waves are calculated by the proposed GFDM and displayed in Fig. 7a and b. It is shown that, for these four incident periods waves, the agreement is excellent among the present numerical solution

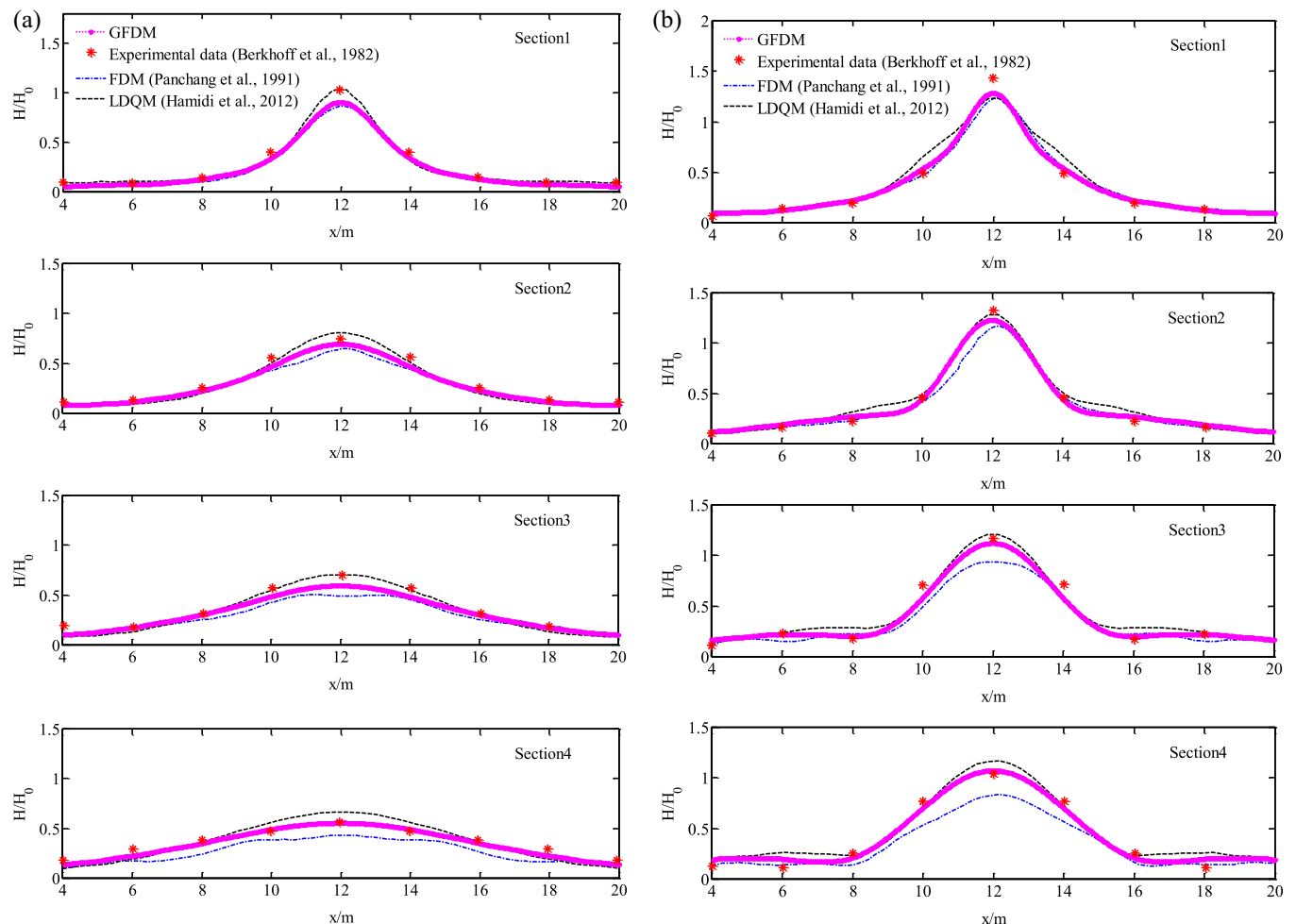


Fig. 14. Linear MSE model results by GFDM in comparison with experimental data and other numerical results. (a) 2 m breakwater gap, and (b) 4 m breakwater gap.

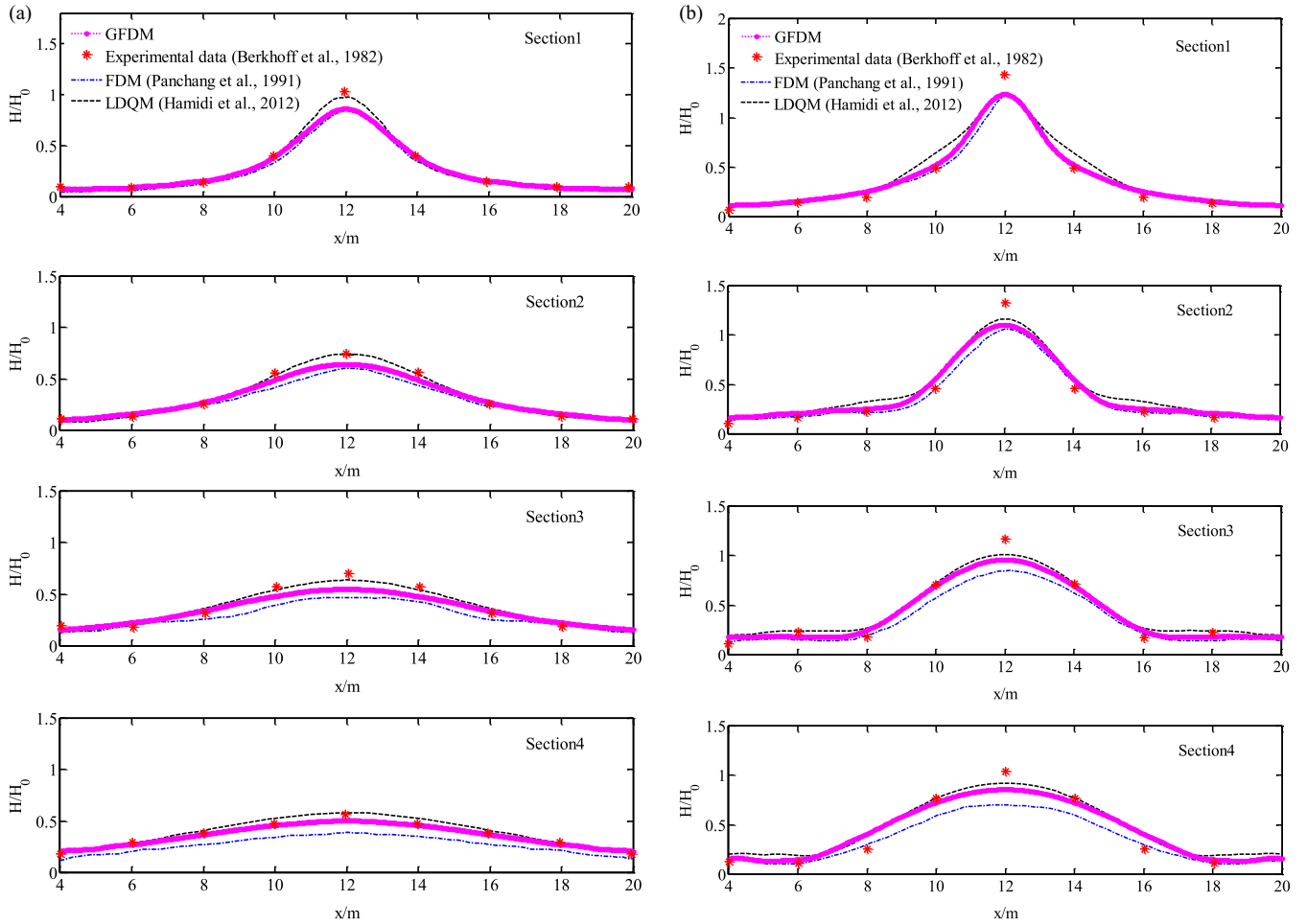


Fig. 15. Nonlinear MSE model results by GFDM in comparison with experimental data and other numerical results. (a) 2 m breakwater gap, and (b) 4 m breakwater gap.

based on the MSE and other solutions to various governing equations. Since Homma's result [48] is based on the LWE, it presents a slightly overestimated result in the range of 100 to 180° for cases of $T=410$ s and $T=480$ s.

For waves with $T=240$ s ($k_a h_a = 0.1772$ and $k_b h_b = 0.5549$), which can be regarded as intermediate waves, the GFDM result is identical with that of other methods except the Homma's analytical solution, which diverges significantly especially in the degrees of 50 to 90 and 100 to 160. The comparative analysis is described in Fig. 7c.

As for the incident wave period decreases to $T=120$ s ($k_a h_a = 0.3601$ and $k_b h_b = 1.2990$), four results by other researchers [49–51,53] are chosen to compare with the proposed GFDM result, which is presented in Fig. 7d. It is exhibited that the present numerical result is almost identical to these four solutions except for tiny discrepancy appear near several peaks and troughs of the Zhu's solution [51].

As described by Liu et al. [49] that the computational cost for most numerical method will substantially increase due to sufficient accuracy for much shorter period of incident wave. Fig. 7e displays the comparison among the present numerical solution and the previous studies for $T=90$ s with $k_a h_a = 0.4882$ and $k_b h_b = 2.0555$. The overall agreement among the GFDM result and other solutions such as Liu's FDM numerical result [49] and series solutions [53] is satisfactory, notwithstanding Zhu's numerical model presenting smaller values at some troughs and higher values for degrees various from 140° to 180°.

The case of $T=60$ s is more complicated than those cases described above for the reason of $k_a h_a = 0.7693$ and $k_b h_b = 4.4772$, which imply that the waves are in the range of the intermediate wave and the short wave with respect to the depth h_a and h_b , respectively. It is conceivable

that this situation is a challenging test for any numerical model since the computational expense increases dramatically as mentioned before. Even so, this case has been studied by several prevenient researchers [49,50,52,53]. It is also investigated by the GFDM and the result is compared with these previous researches as presented in Fig. 7f. It is found that all the results maintain a relatively satisfied agreement although Zhu's GDRBEM model and Liu's FDM model present disparities at range of 120° to 180°. Particularly, the GFDM result is matched nicely with the approximate analytic solution [51] and the series solution [53] and it has never been found before that a numerical model gets such a consistent result with analytical solution for this severe case. Two 3-D dimensional presentations of the present numerical results of $T=240$ s for this example are provided in Fig. 8. The provided results and comparisons in this example verified again the satisfactory feasibility and excellent accuracy of applying the GFDM to solve the MSE.

4.3. Wave propagation over an elliptic shoal

Wave propagation over a submerged elliptic shoal mounted on a slope, of which the experimental setup provided by Berkhoff et al. [43] as shown in Fig. 9, is a classical case for modeling the combined wave refraction and diffraction and has been studied many times [14,16,43,47,54]. This typical case is studied again using the GFDM in this subsection and both linear and nonlinear wave are considered.

As described in Fig. 9, an elliptic shoal of defined geometry is placed on a bottom slope, the gradient of which is 2%. The left incident wave with the amplitude of $a_0 = 0.0232$ m and the period of $T=1$ s is gener-

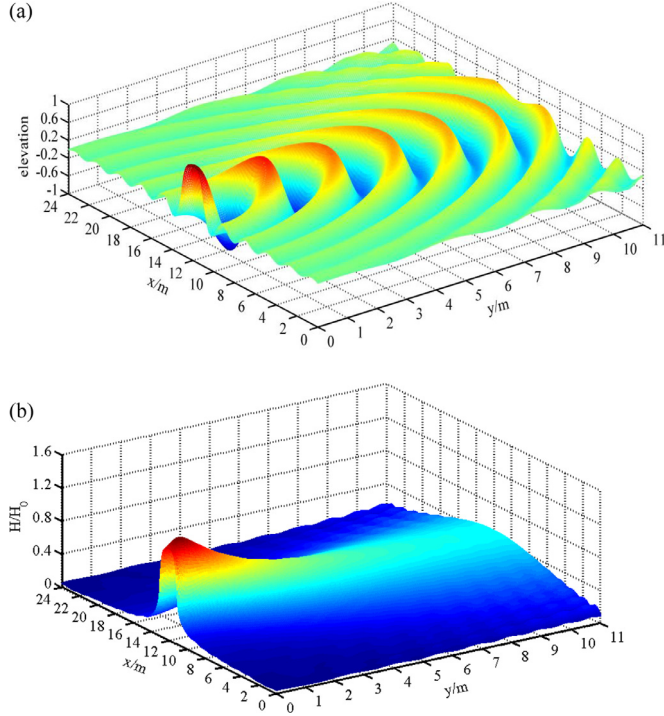


Fig. 16. 3-D presentation of results for 2 m breakwater gap. (a) free surface elevation, and (b) relative wave height.

ated by a wave-maker, which is arranged at $y = -10$ m. The wave propagates across the computational domain to the end boundary at $y = 12$ m.

The slope oriented coordinates (x', y') , as shown in Fig. 9, can be related with the computational coordinates (x, y) by the following equations,

$$\begin{aligned} x' &= (x - x_0) \cos 20^\circ + (y - y_0) \sin 20^\circ \\ y' &= (y - y_0) \cos 20^\circ - (x - x_0) \sin 20^\circ \end{aligned} \quad (36)$$

where $(x_0, y_0) = (0, 0)$ denotes the center of shoal. Then, the position of the shoal is set as,

$$\left(\frac{x'}{4}\right)^2 + \left(\frac{y'}{3}\right)^2 < 1 \quad (37)$$

The water depth out of range of the shoal is given by,

$$\begin{aligned} h_s &= 0.45 - 0.02(5.84 + y') & y' \geq -5.84 \text{ m} \\ h_s &= 0.45 & y' < -5.84 \text{ m} \end{aligned} \quad (38)$$

and the water depth over the shoal is defined as,

$$h = h_s + 0.3 - 0.5 \sqrt{1 - \left(\frac{x'}{5}\right)^2 - \left(\frac{y'}{3.75}\right)^2} \quad (39)$$

As presented in Fig. 10, relative wave heights at eight sections are chosen to confirm that applying the GFDM to the linear MSE is workable and accurate. The present results are in good agreement with the experimental data at Section 1, as well as the remaining sections except for several peaks and troughs. Moreover, the present numerical scheme acquires a considerable agreement with other methods especially the FDM model [14] at most sections. It has been pointed out by previous researchers [14,47] that the FEM solution [43] is restricted to 31% of the physical domain due to computational limitations. Fortunately, the present GFDM model can handle the whole physical domain. Fig. 11 provides a 3-D presentation of the numerical results for linear model.

As mentioned above, there are some mismatches between all the linear models and the experimental data, and this phenomenon is due to

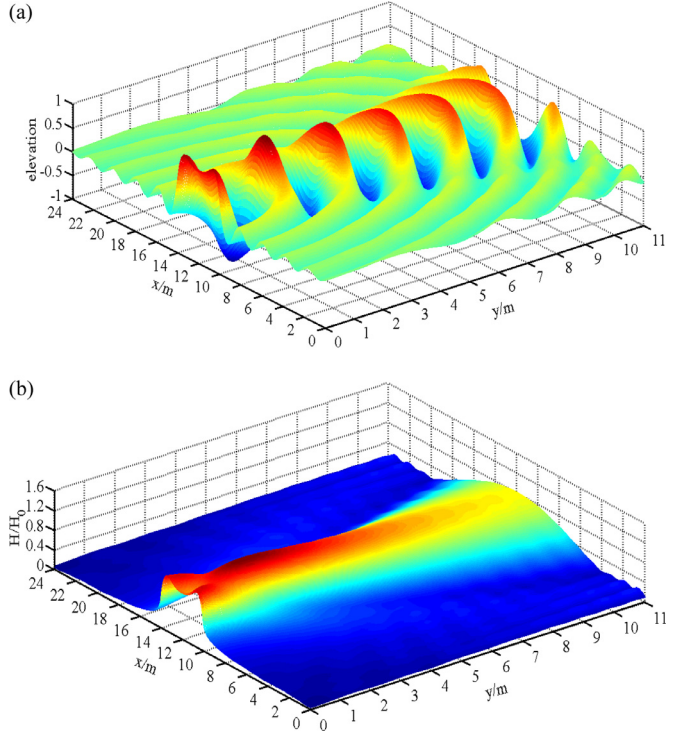


Fig. 17. 3-D presentation of results for 4 m breakwater gap. (a) free surface elevation, and (b) relative wave height.

the superiority of nonlinear effects, as discussed by other researchers [14,39,43,47]. Fig. 12 shows the GFDM results compare with the experimental data [43], the FDM [14] and the LDQM [47] to the nonlinear MSE model, which has been illustrated to bring about a more accurate result. In these figures, significant improvement of the results compared with the linear model is presented for all eight sections, and the GFDM results are nearly identical with the experimental data and other numerical solutions except for overestimate at few parts of the last two sections.

The feasibility of applying the GFDM to the MSE is confirmed by this classical elliptic shoal case. Moreover, solving the nonlinear MSE model with the present algorithm verifies the extensive applicability of the GFDM.

4.4. Single gate breakwater

In 1994, Wu and Xia [55] developed a typical two-dimensional wave model, in which waves are diffracted by a single gate and refracted due to a slant bottom after the gate. This example is considered as the last case in this paper.

As shown in Fig. 13, incident waves, with the period $T = 1.41$ s and the wave height $H_0 = 0.12$ m, propagate over a 24×11 m computational domain. The breakwater is assumed to be fully reflective while totally absorbing boundary conditions are applied at other boundaries. The gradient of the sea bed is 1:50 and the water depth changing with the slope is defined as,

$$h = 0.3 - 0.02y \quad (40)$$

Similar with the experiment setting in [55], both 2 m and 4 m of the breakwater gap for linear and nonlinear MSE models are considered in this paper. In addition to experimental data [55], two numerical algorithms, FDM model [16] and LDQM model [47], are adopted to compare with the proposed GFDM method. The relative wave heights with linear and nonlinear MSE model along four cross sections are presented in Figs. 14 and 15, respectively. As the figures described, both the linear and nonlinear results of the GFDM are fairly consistent with the experimental data and other numerical solutions. In both of Figs. 14 and 15,

the GFDM results are almost identical to other numerical solutions [16,47], which can be used to verify the accuracy of the proposed meshless numerical scheme. Without the needs for orthogonal grids in the FDM and special nodal arrangements in the LDQM, the proposed GFDM-based numerical scheme can accurately and simply acquired similar solutions of the FDM [16] and the LDQM [47]. Although there are some obvious differences between the GFDM results and the experimental data [55] in Figs. 14 and 15, the tendency of the numerical and experimental data are almost the same. This differences between numerical results and experimental data also appears in the comparisons of other papers [16,47]. From the numerical comparisons in Figs. 14 and 15, it can be verified that the proposed GFDM model can effectively obtain accurate results for both of linear and nonlinear MSE models.

Three-dimensional distributions of the relative wave heights and the surface water elevations of the nonlinear mode for 2 m and 4 m breakwater gaps are illustrated in Figs. 16 and 17, respectively. As the pictures reveal, waves enter the computational domain through the breakwater gap and propagate over the whole region. This procedure of wave transformation is mainly attributed to the diffraction effects by the single gate. Then, waves focus slightly at the center line along y-direction behind the single gate. This phenomenon is due to the combined diffraction and refraction effects of the single gate, slope bottom and solid breakwater.

5. Conclusions and discussions

Waves are probably refracted and diffracted when propagated over waters of variable depth or through coastal structures. In this paper, the GFDM, which is a newly developed domain-type meshless method, performs reasonably well in simulating wave reflection and diffraction processes and produces stable and efficient numerical results for practical application. The superiority of the GFDM is that it can avoid the time-consuming and complicated work of generating meshes and numerical quadrature. The partial derivatives of the equation at every node can be derived with the moving-least-squares method of the GFDM and expressed as linear combinations of nearby function values multiplying by corresponding weighting coefficients. In addition, the domain feature of the GFDM contributes to the generation of a sparse system of linear algebraic equations, which leads to high-efficiency of this numerical method.

By comparing the present numerical results with other previous numerical results, analytical solutions and experimental data for four numerical examples provided in this paper, the superior performance of applying the proposed meshless numerical scheme to the MSE are fully vindicated as the satisfying results are obtained. In the first example, different numbers of total points are used to verify the stability of the present scheme. In addition, the MSE models with linear and nonlinear dispersion relations are both studied in the last two examples, and it can be observed from the corresponding numerical results that the nonlinear effect leads to a better result especially for the elliptic shoal model. Obviously, the GFDM can be applied to solve both the linear and nonlinear models efficiently and accurately. A surprising result is obtained in the second example. For the case with $T=60$ s, the present numerical result is almost identical with both Cheng's and Liu's approximate analytic solution [50,53]. This level of consistency between numerical result and analytic solution for this severe case is hard to come by.

Application of the GFDM, combining with a suitable temporal discretization method, for the time-dependent mild slope equation can be studied in future works. Other models, which considering wave breaking and bottom friction, or adding damping terms in the mild slope equation, are also topics of further study.

Acknowledgement

The authors acknowledge gratefully the National Natural Science Foundation of China (Grant No. 51679042) for the financial support to this research.

References

- [1] Berkhoff JCW. Computation of combined refraction-diffraction. In: Proceedings of the 13th international conference on coastal engineering ASCE; 1972. p. 471–90.
- [2] Dalrymple RA, Kirby JT, Hwang PA. Wave diffraction due to areas of energy dissipation. *J Waterway Port Coast Ocean Eng* 1984;110(1):67–79.
- [3] Khellaf MC, Bouhadef M. Modified mild slope equation and open boundary conditions. *Ocean Eng* 2004;31(13):1713–23.
- [4] Zhao HJ, Song ZY, Xu FM, Li RJ. An extended time-dependent numerical model of the mild slope equation with weakly nonlinear amplitude dispersion. *Acta Oceanol Sin* 2010;29(2):5–13.
- [5] Massel SR. Extended refraction-diffraction equation for surface waves. *Coast Eng* 1993;19(1–2):97–126.
- [6] Lee CH, Yoon SB. Effect of higher-order bottom variation terms on the refraction of water waves in the extended mild-slope equations. *Ocean Eng* 2004;31(7):865–82.
- [7] Dally WR, Dean RG, Dalrymple RA. Wave height variation across beaches of arbitrary profile. *J Geophys Res* 1985;90(C6):917–27 11.
- [8] Oliveira FSBF. Numerical modelling of deformation of multi-directional random waves over a varying topography. *Ocean Eng* 2007;34(2):337–42.
- [9] Tang Y, Ouellet Y. A new kind of nonlinear mild-slope equation for combined refraction-diffraction of multi frequency waves. *Coast Eng* 1997;31(1–4):3–36.
- [10] Toledo Y, Agnon Y. Nonlinear refraction/diffraction of water waves: The complementary mild-slope equations. *J Fluid Mech* 2009;641:509–20.
- [11] Lee CH, Suh KD. Internal generation of waves for time-dependent mild slope equations. *Coast Eng* 1998;34(1–2):35–57.
- [12] Kim GW, Lee CH, Suh KD. Generation of random waves in time-dependent extended mild-slope equations using a source function method. *Ocean Eng* 2006;33(14–15):2047–66.
- [13] Beels C, Troch P, De Backer G, Vantorre M, De Rouck J. Numerical implementation and sensitivity analysis of a wave energy converter in a time dependent mild-slope equation model. *Coast Eng* 2010;57(5):471–92.
- [14] Panchang VG, Pearce BR, Wei G, Cushman-Roisin B. Solution of the mild-slope wave problem by iteration. *Appl Ocean Res* 1991;13(4):187–99.
- [15] Li B. A generalized conjugate gradient model for the mild slope equation. *Coast Eng* 1994;23(3–4):215–25.
- [16] Tang J, Shen YM, Zheng YH, Qiu DH. An efficient and flexible computational model for solving the mild slope equation. *Coast Eng* 2004;51(2):143–54.
- [17] Chen W, Panchang V, Demirbilek Z. On the modeling of wave-current interaction using the elliptic mild-slope wave equation. *Ocean Eng* 2005;32(2011):17–18.
- [18] Liu SX, Sun B, Sun ZB, Li JX. Self-adaptive fe numerical modeling of the mild-slope equation. *Appl Math Models* 2008;25(12):2775–91.
- [19] Naserizadeh R, Bingham HB, Noorzad A. A coupled boundary element finite difference solution of the elliptic modified mild slope equation. *Eng Anal Bound Elem* 2011;35(1):25–33.
- [20] Young DL, Lin YC, Fan CM, Chiu CL. The method of fundamental solutions for solving incompressible Navier-Stokes equations. *Eng Anal Bound Elem* 2009;33:1031–44.
- [21] Chen JT, Shieh HC, Lee YT, Lee JW. Bipolar coordinates, image method and the method of fundamental solutions for Green's functions of Laplace problems containing circular boundaries. *Eng Anal Bound Elem* 2011;35:236–43.
- [22] Karunasena HCP, Senadeera W, Brown RJ, Gu YT. Simulation of plant cell shrinkage during drying – A SPH-DEM approach. *Eng Anal Bound Elem* 2014;44:1–18.
- [23] You CF, Qiu Y, Xu XC, Xu DL. Numerical simulations of viscous flows using a meshless method. *Int J Numer Methods Fluids*. 2008;58:727–41.
- [24] Chen YW, Liu CS, Chang CM, Chang JR. Applications of the modified Trefftz method to the simulation of sloshing behaviours. *Eng Anal Bound Elem* 2010;34:581–98.
- [25] Fan CM, Chan HF, Kuo CL, Yeih WC. Numerical solutions of boundary detection problems using modified collocation Trefftz method and exponentially convergent scalar homotopy algorithm. *Eng Anal Bound Elem* 2012;36:2–8.
- [26] Pal P, Bhattacharyya SK. Slosh dynamics of liquid-filled rigid containers: two-dimensional meshless local Petrov-Galerkin approach. *J Eng Mech-ASCE* 2012;138:567–81.
- [27] Chan HF, Fan CM. The local radial basis function collocation method for solving two-dimensional inverse Cauchy problems. *Numer Heat Transf B—Fundam* 2013;63:284–303.
- [28] Benito JJ, Urena F, Gavete L. Influence of several factors in the generalized finite difference method. *Appl Math Model* 2001;25(12):1039–53.
- [29] Benito JJ, Urena F, Gavete L. Solving parabolic and hyperbolic equations by the generalized finite difference method. *J Comput Appl Math* 2007;209:208–33.
- [30] Benito JJ, Urena F, Gavete L, Alonso B. Application of the generalized finite difference method to improve the approximated solution of pdes. *CMES Model Eng Sci* 2008;38:39–58.
- [31] Gavete L, Gavete ML, Benito JJ. Improvements of generalized finite difference method and comparison with other meshless method. *Appl Math Model* 2003;27:1039–53.
- [32] Urena F, Salete E, Benito JJ, Gavete L. Solving third- and fourth-order partial differential equations using GFDM: application to solve problems of plates. *Int J Comput Math* 2012;89:366–76.
- [33] Chan HF, Fan CM, Kuo CW. Generalized finite difference method for solving two-dimensional nonlinear obstacle problems. *Eng Anal Bound Elem* 2013;37:1189–96.
- [34] Fan CM, Huang YK, Li PW, Chiu CL. Application of the generalized finite-difference method to inverse biharmonic boundary-value problems. *Numer Heat Transf B—Fundam* 2014;65:129–54.
- [35] Fan CM, Li PW, Yeih W. Generalized finite difference method for solving two-dimensional inverse Cauchy problems. *Inverse Probl Sci Eng* 2015;23(5):737–59.

- [36] Zhang T, Ren YF, Fan CM, Li PW. Simulation of two-dimensional sloshing phenomenon by generalized finite difference method. *Eng Anal Bound Elem* 2016;63:82–91.
- [37] Zhang T, Ren YF, Yang ZQ, Fan CM. Application of generalized finite difference method to propagation of nonlinear water waves in numerical wave flume. *Ocean Eng* 2016;123:278–90.
- [38] Li PW, Fan CM. Generalized finite difference method for two-dimensional shallow water equations. *Eng Anal Bound Elem* 2017;80:58–71.
- [39] Zhu SP, Liu HW, Chen K. A new DRBEM model for wave refraction and diffraction. *Eng Anal Bound Elem* 1993;12:261–74.
- [40] Kirby JT, Dalrymple RA. An approximate model for nonlinear dispersion in monochromatic wave propagation models. *Coast Eng* 1986;9:545–61.
- [41] Li D. 2002. Los Angeles-long beach harbor pier 400 harbor resonance study using numerical model, CGWAVE. MSc Thesis, University of Maine, USA
- [42] Ureña M, Benito JJ, Ureña F, Salete E, Gavete L. Application of GFDM to reflection and transmission problems in seismic SH waves propagation. *Math Methods Appl Sci* 2017;5:30–7.
- [43] Berkhoff JCW, Booy N, Radder AC. Verification of numerical wave propagation models for simple harmonic linear water waves. *Coast Eng* 1982;6:255–79.
- [44] Kirby JT, Dalrymple RA. Verification of a parabolic equation for propagation of weakly nonlinear waves. *Coast Eng* 1984;8:219–32.
- [45] Bettess P, Zienkiewicz OC. Diffraction and refraction of surface waves using finite and infinite elements. *Int J Numer Methods Eng* 1977;11(8):1271–90.
- [46] Zhang YL, Zhu SP. New solutions for the propagation of long water waves over variable depth. *J Fluid Mech* 1994;278:391–406.
- [47] Hamidi ME, Hashemi MR, Talebbeydokhti N, Neill SP. Numerical modelling of the mild slope equation using localised differential quadrature method. *Ocean Eng* 2012;47:88–103.
- [48] Homma S. On the behaviour of seismic sea waves around circular island. *Geophys Mag* 1950;21:199–208.
- [49] Liu HW, Lin PZ, Jothi Shankar N. An analytic solution for combined refraction and diffraction based on the mild-slope equation. *Coast Eng* 2004;51:421–37.
- [50] Cheng YM. A new solution for waves incident to a circular island on an axi-symmetric shoal. *Ocean Eng* 2011;38:1916–24.
- [51] Zhu SP, Liu HW, Chen K. A general DRBEM model for wave refraction and diffraction. *Eng Anal Bound Elem* 2000;24:377–90.
- [52] Lin PZ. A compact numerical algorithm for solving the time-dependent mild slope equation. *Int J Numer Methods Fluids* 2004;45:625–42.
- [53] Liu HW, Xie JJ. The series solution to the modified mild-slope equation for wave scattering by Homma's island. *Wave Motion* 2013;50:869–84.
- [54] Liu ZB, Zhang RX, Chen B. High order numerical code for hyperbolic mild slope equations with nonlinear dispersion relation. *J Ocean Univ Chin* 2007;6:421–3.
- [55] Wu Y, Xia ZH. 1994. The experimental verification of the numerical model for the two-dimension wave. Report no. COE9405, State Key Laboratory of Coastal and Offshore Engineering, Dalian University of Technology, Dalian, People's Republic of China
- [56] Vastano AC, Reid RO. Tsunami response for islands: verification of a numerical procedure. *J Mar Res* 1967;25:129–39.
- [57] Jonsson IG, Skovgaard O, Brink-Kjaer O. Diffraction and refraction calculations for waves incident on an island. *J Mar Res* 1976;34(3):469–96.
- [58] Houston JR. Combined refraction and diffraction of short waves using the finite element method. *Appl Ocean Res* 1981;3:163–70.
- [59] Tsay TK, Liu PLF. A finite element model for wave refraction and diffraction. *Appl Ocean Res* 1983;5:30–7.